RESEARCH ARTICLE
SPACE PHYSICS: IONOSPHERIC PHYSICS

Earth and Planetary Physics
7: 445–459, 2023
doi: 10.26464/epp2023042

A new strategy for ionospheric remote sensing using the 130.4/135.6 nm airglow intensity ratios

XiaoHan Yin[1], JianQi Qin[1]*, and Larry J. Paxton[2]

[1]School of Earth and Space Sciences, Peking University, Beijing 100871, China;

[2]Applied Physics Laboratory, Johns Hopkins University, Laurel, MD 20723, USA

Key Points:

- Statistical and global characteristics of the 130.4/135.6 nm airglow intensity ratios in the nighttime ionosphere are investigated.
- The intensity ratio observed from 400 km is shown to be a good proxy for the typical peak height of the nighttime ionosphere between ~250 and 450 km.
- An analysis of synthetic observations shows promising results for the use of intensity ratios for global-scale ionospheric remote sensing.

Citation: Yin, X. H., Qin, J. Q., and Paxton, L. J. (2023). A new strategy for ionospheric remote sensing using the 130.4/135.6 nm airglow intensity ratios. *Earth Planet. Phys.*, *7*(4), 445–459. http://doi.org/10.26464/epp2023042

Abstract: We demonstrate here that global-scale determination of a key ionospheric parameter, the peak height of the F_2 region (h_mF_2), can be obtained by making a simple ratio measurement of the atomic oxygen 130.4 and 135.6 nm emissions in the far-ultraviolet nightglow with a nadir-viewing system such as a pair of photometers suitable for flight on a CubeSat. We further demonstrate that measurements from an altitude that is within the typical range of nighttime $h_mF_2 \simeq$ 250–450 km can provide the ratios that are needed for retrieval of the h_mF_2. Our study is conducted mostly through numerical simulations by using radiative transfer models of the two emissions coupled with empirical models of the atmosphere and ionosphere. Modeling results show that the relationship between the h_mF_2 and the intensity ratio is sensitive to the altitude from which the emissions are observed, primarily because of the distinctly different degrees of resonant scattering of the two emissions in the atmosphere. A roughly quadratic relationship can be established for observations from an orbit of ~400 km, which enables h_mF_2 retrieval. Parametric analysis indicates that the relationship can be affected by the ambient atmospheric conditions through resonant scattering and O_2 absorption. For typical nighttime conditions with $h_mF_2 \simeq$ 250–450 km, retrieval of the h_mF_2 from synthetic observations shows that the typical errors are only a few kilometers (up to ~20 km), depending on the accuracy of the ambient conditions predicted by the empirical models. Our findings pave the way for use of the 130.4/135.6 nm intensity ratios for global-scale monitoring of the nighttime ionosphere at mid to low latitudes.

Keywords: nighttime ionosphere; far-ultraviolet remote sensing; 130.4/135.6 nm airglow intensity ratio; peak height of the F_2 region (h_mF_2); TIMED observation

1. Introduction

The resonant lines of atomic oxygen at 130.4 and 135.6 nm are two bright emission features in the far-ultraviolet nightglow (Meier, 1991). The pervasive presence of these emissions over the entire globe makes them excellent proxies for remote sensing of the nighttime ionosphere and thermosphere (Meier, 1991; Stephan et al., 2001; DeMajistre et al., 2005; Zhang YL et al., 2006; Dymond, 2009; Zhang YL and Paxton, 2019; Kil et al., 2020; Wang YG et al., 2022, Sun LC et al., 2021). In the past two decades, space-based observations of these two resonant lines, particularly the 135.6 nm emission, have been used as a primary means for global-scale monitoring of the nighttime ionosphere at mid to low latitudes (DeMajistre et al., 2004; Kil et al., 2004; Fu LP et al., 2015; Qin JQ et al., 2015, 2016; Eastes et al., 2017; Kamalabadi et al., 2018; Wautelet et al., 2019, 2021). In the literature, extensive works have been dedicated to the development of numerical methods for the retrieval of ionospheric parameters from the absolute intensities of these airglow emissions (Meier, 1991; Dymond et al., 1997; Qin JQ et al., 2015). Moreover, the potential use of the 130.4 and 135.6 nm intensity ratios for remote sensing of the nighttime ionosphere has been suggested for decades (Strickland and Anderson, 1977; Meier, 1991; Dymond, 2009).

The primary interest in using the 130.4/135.6 nm intensity ratios has been to estimate the peak height of the F_2 region (h_mF_2) of the nighttime ionosphere from space-based observations viewing in the nadir direction (Meier, 1991; Dymond, 2009; Qin JQ, 2020). Previous modeling works have focused on investigating the feasibility of estimating h_mF_2 by using ratios observed from a geosta-

First author: X. H. Yin, xiaohanyin@stu.pku.edu.cn
Correspondence to: J. Q. Qin, jqqin@pku.edu.cn
Received 17 FEB 2023; Accepted 09 APR 2023.
Accepted article online 30 MAY 2023.

tionary orbit of ~35,786 km or from a low-Earth orbit of ~625 km, both of which are located above the typical range of nighttime $h_mF_2 \simeq 250–450$ km (Lei JH et al., 2005). However, the ratios observed at such high orbits are not very sensitive to the variation in the nighttime h_mF_2, changing only in a small range of ~1–2 (Dymond, 2009; Qin JQ, 2020). Such a small range of variations poses a challenge for instrumentation, which needs a sufficiently large signal-to-noise ratio (SNR) to distinguish those slightly different ratios. Moreover, the solution may not be unique to the retrieval of h_mF_2 because of the small variability in the ratios (Qin JQ, 2020). On the other hand, early observations indicated that the intensity ratios could vary from ~2 to 20 when the spectrometer was observing at lower altitudes of ~420 km (Gérard et al., 1977). How observations from such low altitudes might affect retrieval of the h_mF_2 has not been studied in the literature.

In this work, we investigate the characteristics of the nighttime 130.4/135.6 nm intensity ratios observed from different altitudes through mostly numerical simulations. The purpose is to develop useful observational and numerical strategies for retrieving the nighttime h_mF_2 from the ratios. We demonstrate that global-scale determination of the nighttime h_mF_2 can be obtained by making a simple ratio measurement of the 130.4 and 135.6 nm emissions with a nadir-viewing system such as a pair of photometers suitable for flight on a CubeSat or on space stations. Specifically, we show that the h_mF_2 can be retrieved from the ratios observed from an orbit of ~400 km, which is within the typical range of nighttime $h_mF_2 \simeq 250–450$ km. The retrieval accuracy is higher than those observed from higher orbits (e.g., 625 km) located above the typical range of nighttime h_mF_2. Novel numerical algorithms for the retrieval of h_mF_2 from the ratios are developed during the investigation. Our results provide a new strategy for remote sensing of the nighttime ionosphere by using the 130.4/135.6 nm airglow intensity ratios.

2. Models

In our simulations, we consider two primary source mechanisms of the 130.4 and 135.6 nm emissions in the nighttime ionosphere, namely radiative recombination of O^+ with electrons and mutual neutralization of O^+ with O^- (Meier, 1991; Meléndez-Alvira et al., 1999; Strickland et al., 1999; Qin JQ, 2020). The 130.4 and 135.6 nm emissions associated with geomagnetic storms (Zhang YL et al., 2006) and conjugate photoelectrons (Kil et al., 2020) are not included, so our modeling results represent solely the signatures from the ionospheric plasmas at mid to low latitudes during geomagnetically quiet times, with $Ap \leq 20$. Moreover, to prevent contributions from photoelectron impact excitation near the terminator, we consider only the nighttime ionosphere with solar zenith angles (SZAs) larger than 100°. Table 1 shows the relevant chemical reactions and rate coefficients, which are adapted from Qin JQ (2020, Table 1).

The initial volume emission rates, $4\pi\varepsilon_{135.6}$ and $4\pi\varepsilon_{130.4}$, of the two emissions at a given altitude can be readily calculated as (Qin JQ et al., 2015; Kamalabadi et al., 2018)

$$4\pi\varepsilon_{135.6} = \alpha_{135.6}(T_e) n_e n_{O^+} + \beta_{135.6} k_1 k_2 \frac{n_e n_O n_{O^+}}{k_2 n_{O^+} + k_3 n_O}, \quad (1)$$

$$4\pi\varepsilon_{130.4} = \alpha_{130.4}(T_e) n_e n_{O^+} + \beta_{130.4} k_1 k_2 \frac{n_e n_O n_{O^+}}{k_2 n_{O^+} + k_3 n_O}, \quad (2)$$

where the rate coefficients can be found in Table 1 and T_e, n_e, n_O, and n_{O^+} represent the electron temperature, the electron density, and the densities of O and O^+ at that specific altitude, respectively. In Equations (1) and (2), the first terms and the second terms on the right-hand sides are due to radiative recombination and mutual neutralization, respectively. To calculate the initial volume emission rates at different altitudes, the altitude profiles of T_e, n_e, n_O, and n_{O^+} are needed, which can be obtained from empirical or physical models of the atmosphere and ionosphere.

Those initial photons, once generated, will experience scattering and absorption when they are transported in the atmosphere. Radiative transfer models are needed to simulate these physical processes. In this study, the transport of the 130.4 nm emission is computed by using the Monte Carlo radiative transfer (MCRT) model developed by Qin JQ and Harding (2020) based on the algorithm of Meier and Lee (1982). The MCRT model assumes a non-isothermal atmosphere and uses an angle-dependent partial frequency redistribution function. These rigorous treatments are required for the simulation of optically extremely thick emissions, such as the 130.4 nm emission, which has a vertical optical depth on the order of 10^4–10^5. For the 135.6 nm emission, the radiative transfer model developed by Qin JQ et al. (2015) is used instead of the MCRT model for computational efficiency. The model of Qin JQ et al. (2015) solves the radiative transfer equation by direct discretization of its integral form in a non-isothermal atmosphere, which is derived from first principles with a complete frequency

Table 1. Relevant chemical reactions in the nighttime ionosphere.[a]

Reaction	Rate coefficient ($cm^3 s^{-1}$)	Yield	Ref.
$O^- + e \rightarrow O + h\nu_{135.6}$	$\alpha_{135.6} = 7.3 \times 10^{-13}(1{,}160/T_e)^{0.5}$		M
$O^- + e \rightarrow O + h\nu_{130.4}$	$\alpha_{130.4} = 3.4 \times 10^{-13}(1{,}160/T_e)^{0.5}$		S
$O + e \rightarrow O^- + h\nu'$	$k_1 = 1.3 \times 10^{-15}$		M
$O^+ + O^- \rightarrow O + O^*$	$k_2 = 1.0 \times 10^{-7}$		M
$O^- + O \rightarrow O_2 + e$	$k_3 = 1.4 \times 10^{-10}$	$\beta_{135.6}$=0.54	M
		$\beta_{130.4}$=0.46	S

[a]M, Meléndez-Alvira et al. (1999); S, Strickland et al. (1999). *hν* represents the photons emitted from the reactions.

redistribution. The assumption of a complete frequency redistribution is valid for the 135.6 nm emission because its vertical optical depth is on the order of 1.0. Indeed, the two radiative transfer models produce identical results for the 135.6 nm emission (Qin JQ and Harding, 2020; Figure 1). In these two models, the resonant absorption cross sections are calculated by using the parameters given by Meier (1991, Table IV), and the wavelength- and temperature-dependent O_2 photoabsorption cross sections are obtained from the measurements of Ahmed et al. (1996) and Gibson and Lewis (1996). The NRLMSIS 2.0 model (Emmert et al., 2021) and the International Reference Ionosphere (IRI) 2016 model (Bilitza et al., 2017) are used to generate the atmospheric conditions (i.e., the neutral temperature, T_n, and the O and O_2 density profiles, n_O and n_{O_2}) and the ionospheric conditions (i.e., the electron temperature, T_e, and the electron and O^+ density profiles, n_e and n_{O^+}) that are required for our simulations.

3. Results and Discussion

In this section, we first investigate the statistical and global characteristics of the 130.4/135.6 nm intensity ratios in the nighttime ionosphere during geomagnetically quiet times by using the radiative transfer models of Qin JQ et al. (2015) and Qin JQ and Harding (2020) in conjunction with the NRLMSIS 2.0 model (Emmert et al., 2021) and the IRI 2016 model (Bilitza et al., 2017). The modeling results are examined to investigate the relationship between the nighttime h_mF_2 and the intensity ratios observed from different altitudes. We then investigate the effects of multiple scattering and O_2 absorption on the relationship through a parametric analysis by using the three-parameter Chapman profile. Thereafter, we develop numerical algorithms for the retrieval of h_mF_2 from synthetic observations. Finally, we compare our modeling results with observations by the Global Ultraviolet Imager (GUVI) onboard the Thermosphere Ionosphere Mesosphere Energetics and Dynamics (TIMED) mission.

3.1 Statistical and Global Characteristics of the Intensity Ratios

We first investigate the statistical and global characteristics of the 130.4/135.6 nm intensity ratios observed from different orbits in the nighttime ionosphere. Three representative altitudes, 830, 625, and 400 km, which have been used in many low-Earth orbit missions (e.g., the Defense Meteorological Satellite Program [DMSP] of the U.S. Department of Defense, the TIMED mission of the National Aeronautics and Space Administration [NASA], the Chinese FengYun satellites, the International Space Station, and the Chinese Space Station), are assumed in the simulations. The purpose is to investigate how the relationship between the h_mF_2 and the intensity ratios varies with the altitude from which the emissions are observed. For this investigation, the atmospheric (i.e., T_n, n_O, and n_{O_2}) and ionospheric (i.e., T_e, n_e, and n_{O^+}) conditions are specified by using the NRLMSIS 2.0 and IRI 2016 models for geographic latitudes between 45°S and 45°N at 00:00 local time (LT) on March 7, 2002, with a geographical resolution of 5° in both the latitudinal and longitudinal directions (i.e., a total of $19 \times 72 =$ 1,368 individual locations). These locations and times are associated with SZAs of ~130°–180° and day of year (DOY) 66 in 2002 (i.e., 2002066). For this specific day, the daily $F_{10.7}$ flux and its 81-day mean value are 177 and 200 solar flux units (sfu), respectively, and the *Ap* index is 9. The resulting atmospheric and ionospheric conditions are used by the radiative transfer models to simulate a total of 1,368 intensity ratios observed in the nadir direction. For comparison, another set of simulation results are obtained by using the same method explained above, except that the atmospheric and ionospheric conditions are specified by using the thermosphere–ionosphere–electrodynamic general circulation model (TIEGCM; Qian LY et al., 2013).

Figure 1 presents the statistical characteristics of the modeled 130.4/135.6 nm intensity ratios observed in the nadir direction from altitudes of 830, 625, and 400 km. In Figures 1a–c the atmospheric and ionospheric conditions are specified by using the NRLMSIS 2.0 and IRI 2016 models, whereas in Figures 1d–f the conditions are specified by using the TIEGCM. Both the upper and lower panels show that the 130.4/135.6 nm intensity ratios tend to increase with decreasing altitude of the observer and that the intensity ratios and h_mF_2 exhibit a roughly quadratic relationship, especially when the observer is orbiting at 400 km. In the upper panels, the mean ratios for the three orbits are (830) 1.66, (625) 1.79, and (400) 4.16, respectively. In the lower panels, the mean ratios are (830) 1.64, (625) 1.72, and (400) 3.93. By comparing the upper and lower panels, we see that the two sets of results are similar. Moreover, the large ratios for the orbit of 400 km are consistent with those obtained in the early observations of the Ogo-4 satellite (Gérard et al., 1977). The authors explained that the ratios are large because for such a low altitude, an important fraction of the ionosphere is located above the observer and does not contribute to the 135.6 nm emission observed in the nadir direction. On the other hand, the large opacity of the atmosphere to the 130.4 nm emission leads to a much slower decrease in this emission with increasing altitude such that the 130.4/135.6 nm intensity ratios can be as large as ~10 if they are observed from inside the ionosphere. This explanation is demonstrated in Section 3.2. Moreover, in Figure 1 the distributions exhibit elbow shapes (i.e., some intensity ratios are relatively larger than others for h_mF_2 near 330 km; see the red circles), which is explained after the discussion of Figure 2.

Figure 2 presents the global characteristics of the modeled 130.4/135.6 nm intensity ratios observed in the nadir direction from 625 and 400 km. The simulation results shown in Figures 2a–e are identical to those shown in Figures 1a–c and are modeled with the same atmospheric and ionospheric conditions specified by using the NRLMSIS 2.0 and IRI 2016 models. Figures 2a, b present the peak density (n_mF_2) of the ionosphere and the modeled nadir intensities of the 135.6 nm emission. The remarkable resemblance of their global distributions indicates that the nadir intensity of the 135.6 nm emission is a good proxy for the n_mF_2 of the nighttime ionosphere, as has been demonstrated previously (Rajesh et al., 2011; Qin JQ, 2020). Figures 2c, d present the global distributions of the h_mF_2 and the modeled 130.4/135.6 nm intensity ratios observed at 400 km. These two panels show a strong resemblance of the global h_mF_2 distribution to the 130.4/135.6 nm intensity ratios. For comparison, Figure 2e presents the global distribution of the nadir intensity ratios observed from 625 km, in which the regions associated with large intensity ratios are different from those associated with large h_mF_2 (e.g., the regions near 45°S and

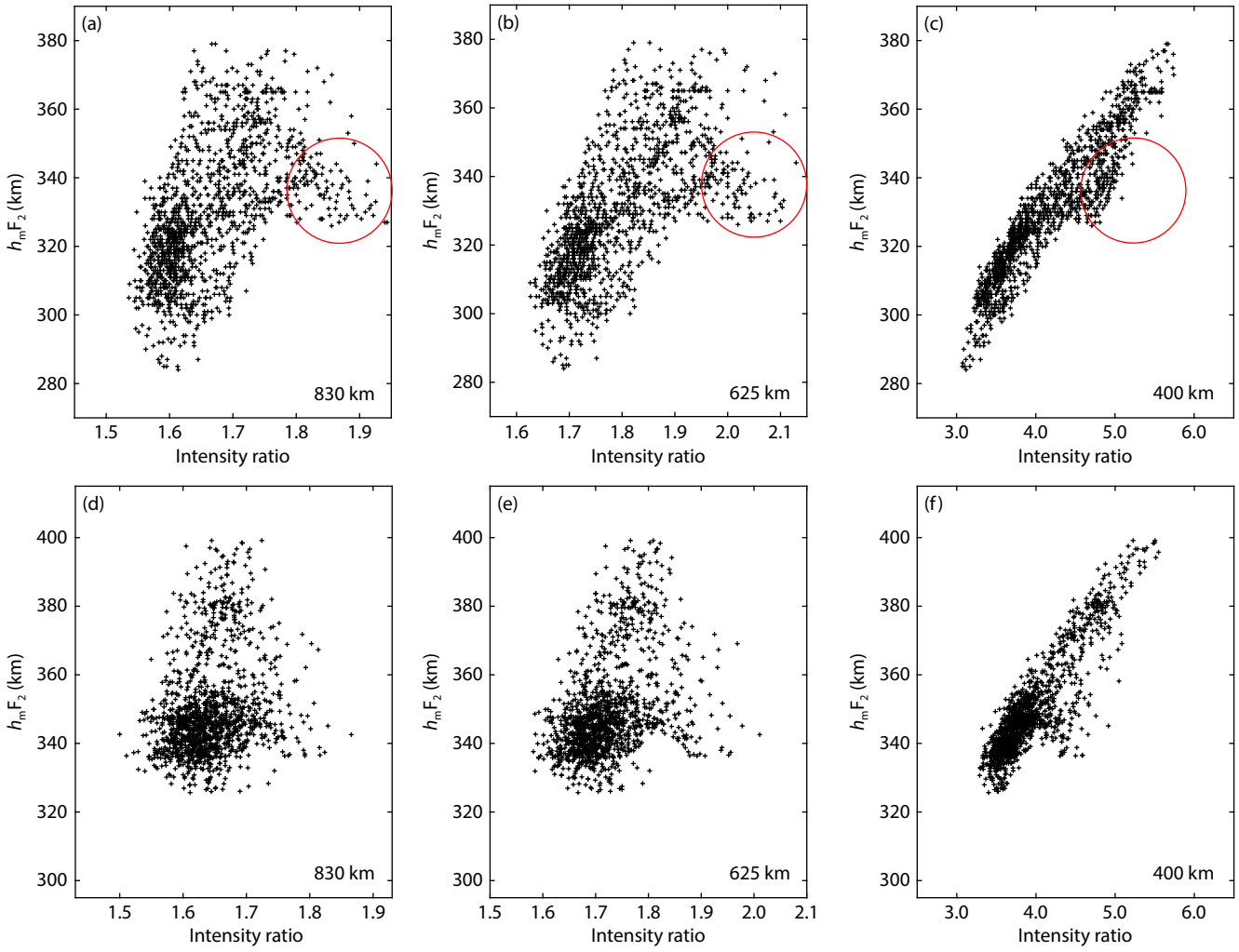

Figure 1. Statistical characteristics of the modeled intensity ratios. (a–c) The relationship between the peak height of the F_2 region (h_mF_2) and the modeled intensity ratios observed in the nadir direction on March 7, 2002, 00:00 local time (LT), from (a) 830 km, (b) 625 km, and (c) 400 km. In these simulations, the atmospheric and ionospheric conditions are specified by using the NRLMSIS 2.0 and IRI 2016 models. The red circles include the relatively large ratios that lead to the elbow shapes. (d–f) Same as (a–c), except that the atmospheric and ionospheric conditions are specified by using the thermosphere–ionosphere–electrodynamic general circulation model (TIEGCM).

45°N). Moreover, in Figure 2e the intensity ratios change only slightly from ~1.7 to 2.1, and the variability is much smaller than those (~3.0–6.0) shown in Figure 2d. This result indicates that observation from 400 km is a better proxy than observation from 625 km for the nighttime h_mF_2, as is demonstrated in Section 3.3. The similarities and differences shown in Figures 2a–e are common. They are further illustrated in Figures 2f–j and are associated with 2002066 03:00 LT. In Figures 2i, j, the morphological differences between the intensity ratios observed from 400 and 625 km can be more clearly seen.

From the results shown in Figures 2c, h, we find that the h_mF_2 predicted by the IRI 2016 model exhibits a latitudinal dependence (i.e., the h_mF_2 is lower in the equatorial region and higher at mid to high latitudes). Because the intensity ratios and the h_mF_2 have a roughly quadratic relationship (see Figure 1), the intensity ratios also exhibit a latitudinal dependence. In other words, the latitudinal dependence of the intensity ratios is an optical manifestation of the latitudinal dependence of the h_mF_2. By comparing Figures 2d, i and 2e, j, we find that the equatorial deeps of the ratios are less obvious if they are observed from a higher orbit (e.g., 400 km versus 625 km).

We now explain the elbow shapes shown in Figure 1. The presence of these elbows is due to the differences in the relative contributions of radiative recombination and mutual neutralization to the emissions. For a given h_mF_2, the 130.4/135.6 nm intensity ratio increases with a larger relative contribution of mutual neutralization, since mutual neutralization leads to a larger emission ratio (0.46/0.54 = 0.85) than does radiative recombination (3.4/7.3 = 0.47; see Table 1). More specifically, when we examine the geographic locations of those relatively large ratios circled in Figure 1, we find that they are associated with the two regions marked by the rectangles in Figure 2, namely the region with latitudes of ~30°N–45°N and longitudes of ~180°–300° and the region with latitudes of ~30°S–45°S and longitudes of ~0°–180°. In these two regions, the h_mF_2 are ~330 km and the n_mF_2 are extremely small, ~2 × 10^5 cm^{-3} (see Figures 2a, c). Such small values of n_mF_2 lead to small relative contributions of radiative recombination such that the intensity ratios are larger than in the

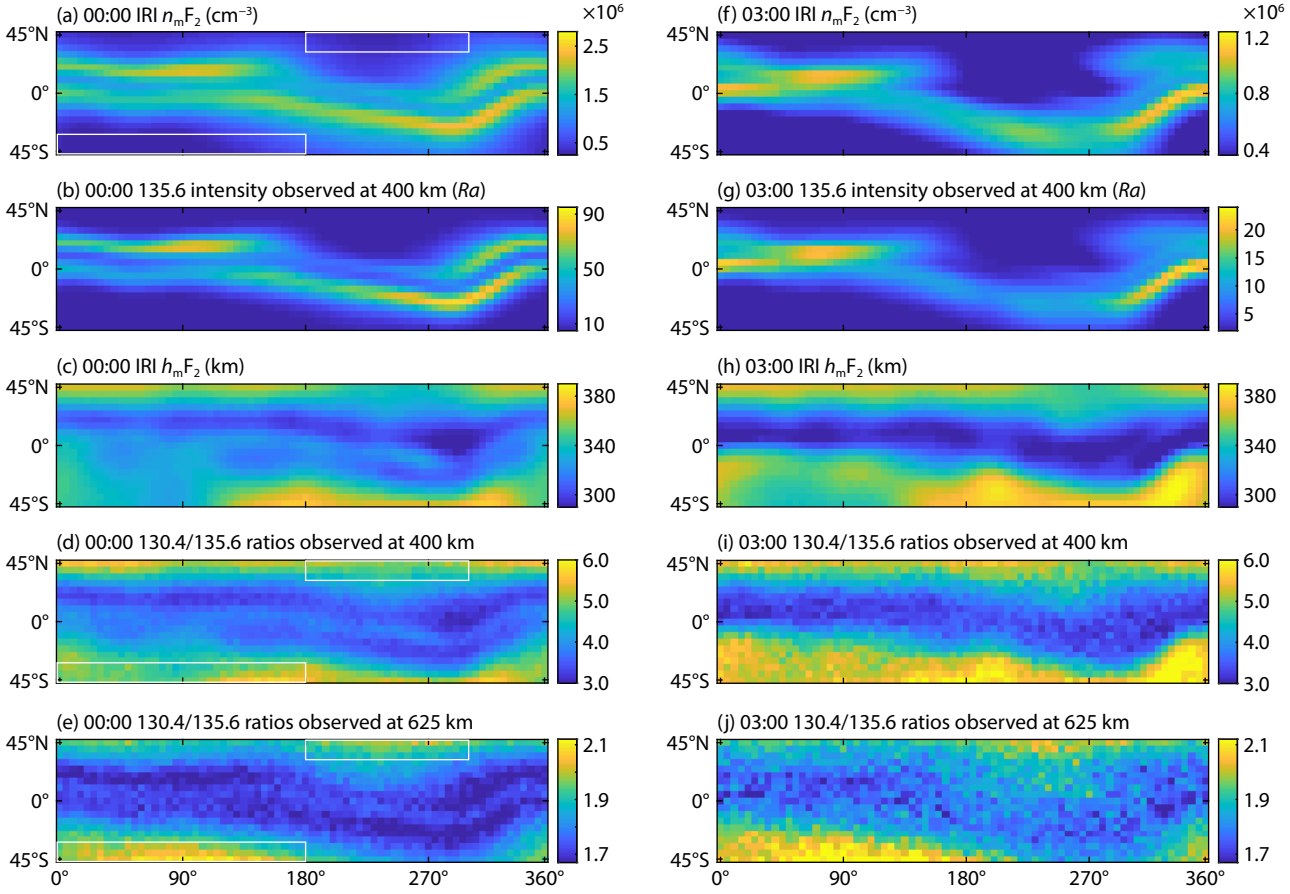

Figure 2. Global characteristics of the modeled intensity ratios. (a–e) Global characteristics of the nighttime ionosphere on March 7, 2002, 00:00 local time (LT), and the modeled 130.4/135.6 nm intensity ratios at mid to low latitudes. (a, c) The peak density (n_mF_2) and peak height of the F_2 region (h_mF_2) of the ionosphere, which are specified by using the International Reference Ionosphere (IRI) 2016 model. (b) The nadir intensities of the 135.6 nm emission in unit of Rayleigh (*Ra*) that are observed from 400 km. (d, e) The 130.4/135.6 nm intensity ratios observed from 400 and 625 km, respectively. The white rectangles indicate the region associated with the relatively large ratios that are circled in Figure 1. (f–j) Same as (a–e), except for 03:00 LT.

other regions with similar h_mF_2 (see Figures 2d, e).

We have also verified that the use of the TIEGCM for specification of the atmospheric and ionospheric conditions leads to similar results as those shown in Figure 2. However, in the rest of our analysis, we use the NRLMSIS 2.0 and IRI 2016 empirical models instead of the TIEGCM to specify the atmospheric and ionospheric conditions for h_mF_2 retrieval. This is done for two reasons. First, the TIEGCM is computationally much more expensive than the empirical models. Because our analyses involve a large number of simulations, high computational efficiency is required. Second, the TIEGCM enforces strong physical constraints on its simulations, which is very useful when it is used as a forward model to theoretically investigate the atmospheric variations under various assumptions. However, when the TIEGCM is used for h_mF_2 retrieval, those physical constraints can strongly limit the solution space such that the solution can be significantly biased in the case when the atmosphere deviates from those assumptions. For this reason, the empirical models that are based on actual measurements are more suitable for h_mF_2 retrieval. In the future when the required observations are available, we can use either the empirical models or the physical models to specify the atmospheric conditions for the retrieval of h_mF_2 from real data and then examine their accuracy by comparison with ionosonde and incoherent scatter radar measurements.

3.2 Effects of Multiple Scattering and O_2 Absorption on the Ratios

As first suggested by Gérard et al. (1977), a correlation should exist between the nighttime h_mF_2 and the 130.4/135.6 nm intensity ratio, primarily because the two emissions undergo distinctly different degrees of resonant scattering in the atmosphere (i.e., the effect of optical trapping on the 130.4 nm emission is orders of magnitude more severe than that of the 135.6 nm emission). In Section 3.1, we demonstrate that a roughly quadratic relationship does indeed exist between the nighttime h_mF_2 and the intensity ratios. As shown in Figure 1, the quadratic relationship is particularly clear if the intensity ratios are observed from an altitude of 400 km, which is within the typical range of nighttime h_mF_2 ≃ 250–450 km (Lei JH et al., 2005). For an observer at a 400 km altitude, a significant portion of the ionosphere is located above the observer such that a slight change in the h_mF_2 can lead to a considerable change in the intensity ratio. Again, this is because of the distinctly different degrees of resonant scattering of the

two emissions in the atmosphere: Most of the 135.6 nm photons that originate above the observer cannot be captured by the observer looking in the nadir direction, whereas a significant number of the 130.4 nm photons that originate above the observer can be captured because of the much stronger effect of multiple scattering (i.e., many of those 130.4 nm photons that originate above the observer can be scattered backward into the field of view when they are transported downward). As a result, a change in the h_mF_2 (i.e., a change in the fraction of the ionosphere that is located above the observer) has a much smaller effect on the intensity of the 130.4 nm emission than does that of the 135.6 nm emission, leading to a change in the intensity ratio. Such a relationship enables the retrieval of h_mF_2 from the intensity ratios.

To further explain the effect of multiple scattering (as well as that of O_2 absorption) on the relationship between the h_mF_2 and the intensity ratios, we perform a parametric study by using the three-parameter Chapman profile:

$$n_e(h) = n_{O^+}(h) = n_mF_2 \times \exp\left[\frac{1}{2} - \frac{h - h_mF_2}{2H} - \frac{1}{2}\exp\left(-\frac{h - h_mF_2}{H}\right)\right], \quad (3)$$

where H is the Chapman scale height and h is the altitude of interest. The ambient atmospheric conditions (i.e., the neutral temperature and the O and O_2 density profiles) are specified by using the NRLMSIS 2.0 model. The Chapman profile is used instead of the IRI 2016 model to represent the ionospheric densities to make the parametric analysis more tractable. In this way, we can readily fix the ambient atmospheric conditions and adjust the three parameters to investigate parametrically the radiative transfer effects on the intensity ratios. For this analysis, n_mF_2 and H are fixed at 1.0×10^6 cm^{-3} and 50 km, respectively. The other parameter, h_mF_2, varies from 250 to 430 km, with a 20 km increment. The ambient conditions are specified by using the NRLMSIS 2.0 and IRI 2016 models at 00:00 LT and [0°N, 0°E] for DOYs 2002066 and 2006194. The solar activity was high on 2002066, as indicated by the daily $F_{10.7}$ flux and its 81-day mean value, which were 177 sfu and 200 sfu, respectively. The geomagnetic activity was weak, with an Ap index of 9. On 2006194, the daily $F_{10.7}$ flux and its 81-day mean value were 72 sfu and 77 sfu, respectively, and the Ap index was 5. We use these two DOYs with minimum and maximum solar activities to generate two very different sets of atmospheric conditions to investigate the effects of multiple scattering and O_2 absorption and to compare the intensity ratios associated with the two solar extremes. Table 2 shows the model atmospheres listing the temperatures and densities at six different altitudes. For the case of 2002066, T_n, T_e, n_O, and n_{O_2} at 600 km are 1,297 K, 1,030 K, 8.26×10^6 cm^{-3}, and 1.75×10^2 cm$^{-3,}$ respectively. In comparison, the values are 869 K, 670 K, 1.07×10^5 cm^{-3}, and 2.84×10^{-1} cm^{-3} for the case of 2006194.

Figures 3a, b present the nadir intensity ratios observed from 400 and 625 km for various h_mF_2. We first model the intensity ratios by using the atmospheric conditions associated with 2002066 00:00 LT at [0°N, 0°E] (the circles). We then replace T_n and n_O with those of 2006194 00:00 LT at [0°N, 0°E] and repeat the simulations (the triangles) to investigate the effect of multiple scattering by O. Further, we replace n_{O_2} by that of 2006194 00:00 LT at [0°N, 0°E] and repeat the simulations again (the squares) to investigate the effect of pure absorption by O_2. The differences between the intensity ratios associated with the two solar extremes can be seen by comparing the circles and squares. These results show that multiple scattering by O affects the intensity ratios more significantly than does pure absorption by O_2. Moreover, both effects are more significant for a higher h_mF_2. To better understand these effects, we calculate the contribution functions of the intensities, which describe how much of the intensity is due to the source photons that originate from each altitude in units of Rayleighs per kilometer. The results are shown in Figures 3c, d. For these calculations, the h_mF_2 is set to 400 km and the ambient conditions are associated with 2002066 00:00 LT at [0°N, 0°E].

The effect of multiple scattering can be understood by comparing the magnitudes and shapes of the contribution functions. First, the contribution functions of the 130.4 nm emission have larger magnitudes than do those of the 135.6 nm emission. Note that the source emission rates of the 130.4 nm photons are roughly half those of the 135.6 nm photons (see Table 1). Also note that 135.6 nm ($^3P_{2,1}$–$^5S_2$) is a spin-forbidden transition, whereas 130.4 nm ($^3P_{2,1,0}$–$^3S_1$) is an electric dipole-allowed transition such that the effect of multiple scattering is much more severe for the latter. Indeed, the magnitudes of the 130.4 nm contribution functions are larger because the effect of optical trapping is orders of magnitude stronger for this emission (Meier, 1991, Table IV). As a result, the 130.4 nm photons encounter very thick atomic oxygen "walls" if they travel in the horizontal and nadir directions so that most of them are forced to escape in the zenith direction, significantly enhancing the nadir intensities. In comparison, the effect of multiple scattering is much weaker for the 135.6 nm emission. In

Table 2. Temperature and density profiles at 00:00 local time and [0°N, 0°E] for 2002066/2006194.[a]

Altitude (km)	T_e (K)	T_n (K)	n_O (cm^{-3})	n_{O_2} (cm^{-3})
600	1,297/869	1,030/670	8.26/0.11 × 10^6	17.5/0.03 × 10^1
450	1,147/842	1,030/670	8.55/0.37 × 10^7	18.7/0.34 × 10^3
300	1,023/781	1,023/669	9.93/1.51 × 10^8	2.51/0.57 × 10^6
200	943/658	943/652	6.18/2.05 × 10^9	0.94/1.04 × 10^8
150	714/567	714/560	2.32/0.98 × 10^{10}	1.46/2.26 × 10^9
100	191/178	191/178	7.14/4.75 × 10^{11}	2.52/2.12 × 10^{12}

[a]Read 8.26/0.11 × 10^6 as 8.26 × 10^6/0.11 × 10^6. 2002066, day of year 66 in 2002; 2006194, day of year 194 in 2006.

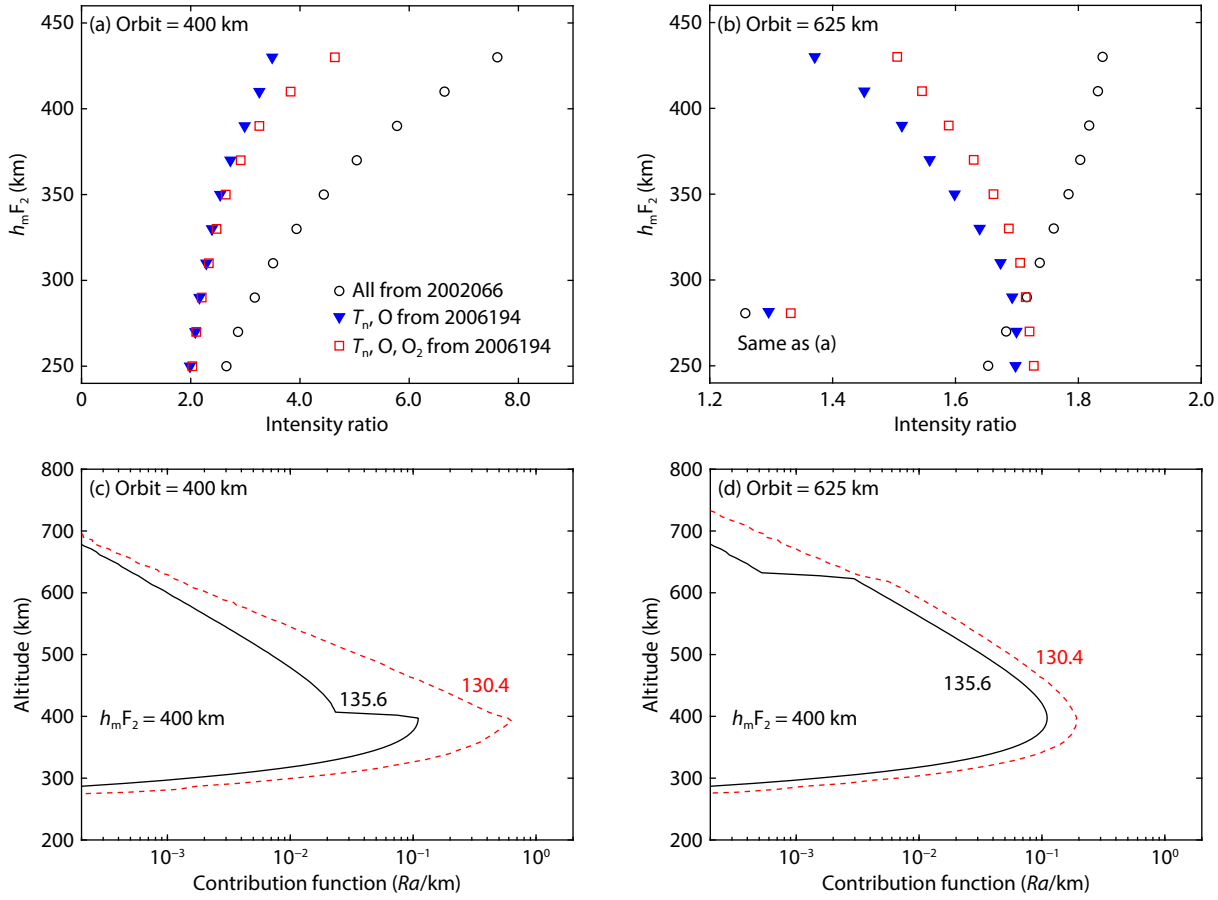

Figure 3. Parametric study using the three-parameter Chapman profile. (a) The intensity ratios observed from 400 km for various peak heights of the F_2 region (h_mF_2). In these simulations, the ambient conditions (i.e., T_n, T_e, n_O, and n_{O_2}) are specified by using the NRLMSIS 2.0 and IRI 2016 models at 00:00 local time and [0°N, 0°E] for days of year (DOYs) 2002066 and 2006194. Circles: T_n, T_e, n_O, and n_{O_2} are all associated with 2002066. Triangles: T_n and n_O are replaced by those of 2006194 to investigate the effect of multiple scattering. Squares: O_2 is replaced by that of 2006194 to investigate the effect of O_2 absorption. (b) Same as (a), except that the intensity ratios are observed from 625 km. (c–d) Contribution functions of the nadir intensities in unit of Rayleigh per kilometer (*Ra*/km) observed at (c) 400 km and (d) 625 km in the case of h_mF_2 of 400 km. The discontinuity in the 135.6 nm contribution function arises from the lack of sufficient backscatter above the observer (see discussion in Section 3.2).

the case shown in Figures 3c, d nearly 99% of the 130.4 nm photons escape upward into space, whereas for the 135.6 nm photons, only ~60% escape. The rest of the photons are absorbed by O_2 in the lower thermosphere. Second, because the atmosphere is relatively optically thin to the 135.6 nm photons, sharp decreases in the contribution functions occur just above the altitude of the orbits (i.e., 400 and 625 km in Figures 3c, d, respectively). In comparison, the decreases are not as evident for the 130.4 nm emission because of the much stronger effect of multiple scattering. Therefore, the intensity ratios for the orbit of 400 km are larger than those for the orbit of 625 km, given that in the former case, a larger portion of the ionosphere is located above the observer.

We next explain why the effect of multiple scattering on the ratios is larger for a higher h_mF_2. For the range of h_mF_2 used in Figures 3a, b, the change in the O density profile only slightly (~10%) reduces the nadir intensities of the 135.6 nm emission. In contrast, the nadir intensities of the 130.4 nm emission are reduced by a factor of 1.5–2.4. This reduction factor is larger for a higher h_mF_2 because of the stronger dependence of the nadir intensities on multiple scattering (i.e., for a higher h_mF_2, more photons originate above the orbits, so the nadir intensities are more sensitive to multiple scattering). In brief, multiple scattering has a much stronger effect on the 130.4 nm emission than on the 135.6 nm emission, so their intensity ratios can be affected significantly by the changes in the O density.

Moreover, in Figures 3a, b the change in O_2 density profile from the one associated with 2002066 to that of 2006194 leads to larger intensity ratios, particularly in the cases of large h_mF_2 (see the triangles and squares). Note that the photoabsorption cross sections of the 135.6 nm emission by O_2 (~6.5×10^{-18} cm^2 at 700 K) are more than an order of magnitude larger than those of the 130.4 nm emission (~4.5×10^{-19} cm^2 at 700 K; Gibson and Lewis, 1996; Ahmed et al., 1996; Figure 4). As a result, the effect of O_2 absorption on the 130.4 nm emission is much weaker than that on the 135.6 nm emission. In our simulations, we have found that the increase in the ratios with the change in n_{O_2} is mostly due to the decrease in the 135.6 nm intensities (whereas the 130.4 nm inten-

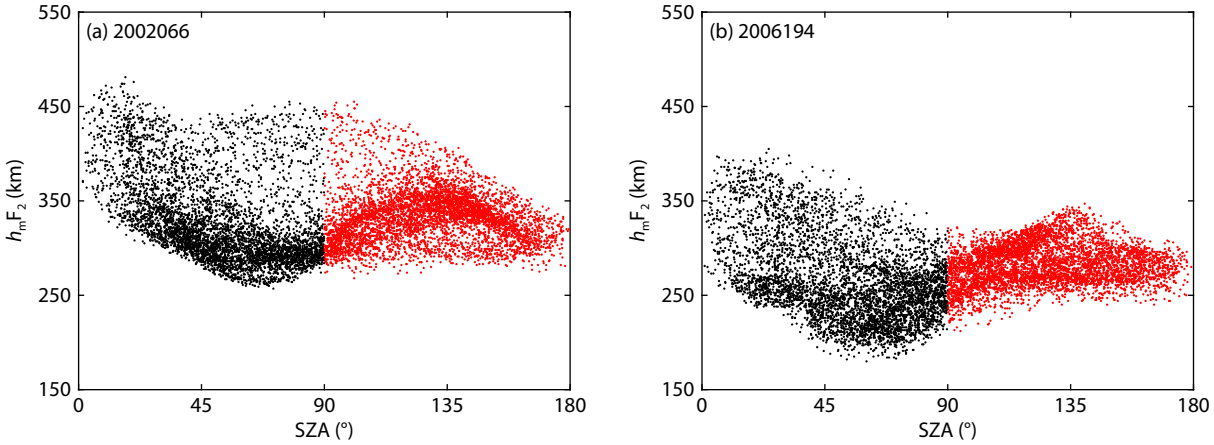

Figure 4. Variability in the peak height of the F_2 region (h_mF_2) on 2002066 and 2006194 at different solar zenith angles (SZAs). For each of the 2 days, a total of 10,000 h_mF_2 were calculated by using the International Reference Ionosphere (IRI) 2016 model for random geographic locations and time. Black: dayside; red: nightside.

sities are barely changed). The decrease in the 135.6 nm intensities might be counterintuitive because one might expect that the O_2 densities associated with minimum solar activity on 2006194 would be lower than those associated with maximum solar activity on 2002066 (thus less photoabsorption). We have examined the two O_2 density profiles and found that the O_2 densities associated with 2006194 are indeed much smaller at altitudes above ~200 km (see Table 2). However, below ~200 km, particularly near ~150 km, the O_2 densities are ~55% larger on 2006194. On the one hand, the vertical optical depth above ~200 km is changed only slightly from 1.3×10^{-3} to 1.0×10^{-3} because of the decrease in O_2 densities, which has a negligible effect on the 135.6 nm emission. On the other hand, the increase in O_2 densities below ~200 km leads to an increase in the vertical optical depth between ~110 and 200 km from ~1.00 to 1.07. According to Qin JQ et al. (2015, Figure 4), the 135.6 nm photons that are originally propagating downward can be scattered back to high altitudes mostly from the region between ~110 and 200 km, which can enhance the nadir intensities. The increase in O_2 absorption in this region weakens the intensity enhancement because fewer photons can be scattered back. This weakening effect is responsible for the increase in the intensity ratios with the change in the O_2 density profile. For a higher h_mF_2, resonant scattering accounts for a larger percentage of the 135.6 nm nadir intensities, so the weakening effect leads to a larger increase in the intensity ratios, as shown in Figures 3a, b. The analysis above indicates that the effect of O_2 absorption on the intensity ratios mostly depends on the O_2 densities below ~200 km.

In brief, we find that the 130.4/135.6 nm intensity ratios can be affected by the ambient atmospheric conditions because the two emissions are affected by resonant scattering to different degrees (about five orders of magnitude higher for the 130.4 nm emission) and by pure absorption to different degrees (about one order of magnitude higher for the 135.6 nm emission). As a result, changes in the atmospheric conditions (i.e., changes in the number densities of O and O_2) can lead to changes in the 130.4/135.6 nm intensity ratios under the same ionospheric conditions (e.g., the same n_mF_2 and h_mF_2).

3.3 Retrieval of h_mF_2 from the Intensity Ratios

Previous modeling studies have shown that the nighttime h_mF_2 can be retrieved from space-based observations of the 130.4/135.6 nm intensity ratios in the nadir direction (Meier, 1991; Dymond, 2009; Qin JQ, 2020). However, those modeling studies have indicated that the intensity ratios observed from a geostationary orbit or from a low-Earth orbit of 625 km have a small variability of ~1–2 and that each ratio can be associated with a large range of h_mF_2 (e.g., for an orbit of 625 km, the intensity ratio of 1.8 can be associated with $h_mF_2 \simeq$ 300–380 km; see Figure 1b). As a result, the estimated h_mF_2 have large errors of tens of kilometers (Dymond, 2009; Qin JQ, 2020). Note that the geostationary orbit and the low-Earth orbit of 625 km are both located above the typical $h_mF_2 \simeq$ 250–450 km in the nighttime ionosphere (Lei JH et al., 2005). Indeed, in Figure 4 we show the variability of the h_mF_2 during high (2002066) and low (2006194) solar conditions, which is calculated by using the IRI 2016 model. The model-predicted variability of $h_mF_2 \simeq$ 250–450 km is consistent with that measured by incoherent scatter radar and ionosonde (Lei JH et al., 2005).

In this section, we describe the development of numerical methods to demonstrate that under typical nighttime conditions, the h_mF_2 can be retrieved more accurately from intensity ratios measured from a low-Earth orbit within the range of ~250–450 km. For such an orbit, a significant fraction of the ionosphere is located above the observer, so the intensity ratio is more sensitive to the variation in h_mF_2 compared with higher orbits (see discussion in Section 3.2). We have chosen an orbit of 400 km for our demonstration because this is near the lower limit of the commonly used low-Earth orbits (e.g., the International Space Station, the Chinese Space Station, and the FengYun 3G satellite). We have also verified that the use of even lower orbits (e.g., 350 km) leads to the same conclusion made in this section. In the following paragraphs, we explain our h_mF_2 retrieval methods and results.

The retrieval of h_mF_2 from a single intensity ratio (or from the two intensities) is a severely underdetermined inverse problem because the ratio depends not only on the h_mF_2, but also on many other highly variable atmospheric conditions (e.g., the O and O_2 densities, the O^+ and electron densities, and the neutral and elec-

tron temperatures; see Section 3.2). To retrieve the h_mF_2, we need to establish an empirical relationship between the h_mF_2 and the ratio under given atmospheric conditions. However, in practice we do not have real-time measurements of those atmospheric conditions, so we have to rely on empirical models (e.g., the NRLMSIS 2.0 and the IRI 2016 models) to predict those conditions for retrieval of the h_mF_2. Inevitably, the use of those model predictions will introduce uncertainties in the h_mF_2 retrieved from real data because of the differences between the predicted and the actual conditions at the time of the observations. For this reason, in the following demonstrations we also assume that the atmospheric conditions are not known accurately, to investigate their effects on h_mF_2 retrieval from synthetic observations. Two retrieval algorithms are developed, which are named the quadratic polynomial fitting (QPF) method and the table lookup method.

3.3.1 The QPF method

We first present the results of the QPF method in Figure 5. In this method, we assume that under given atmospheric conditions, the relationship between the h_mF_2 and the ratio can be described by using a quadratic polynomial, based on the results shown in Figure 1. Specifically, we establish an empirical relationship between the h_mF_2 and the ratio by fitting the modeled intensity ratios using a quadratic polynomial. Any measured ratios can then be readily converted to the h_mF_2 by using the quadratic polynomial. The accuracy of the retrieval depends on how the modeled ratios scatter around the quadratic polynomial. To further explain the details of the QPF method, as shown in Figures 5a–c, we retrieve the h_mF_2 from a single modeled intensity ratio, which is generated by using the atmospheric and ionospheric conditions specified by the NRLMSIS 2.0 and IRI 2016 models on 2002066 00:00 LT at [0°N, 0°E]. The observer is assumed to orbit at 400 km. Under these conditions, the true h_mF_2 is 339 km, and the true intensity ratio is 4.07. Assuming that we have observed a ratio of 4.07 at the aforementioned location and time, our goal is to estimate the h_mF_2 from the ratio as accurately as possible.

To derive the h_mF_2 from the observed ratio, we first calculate the

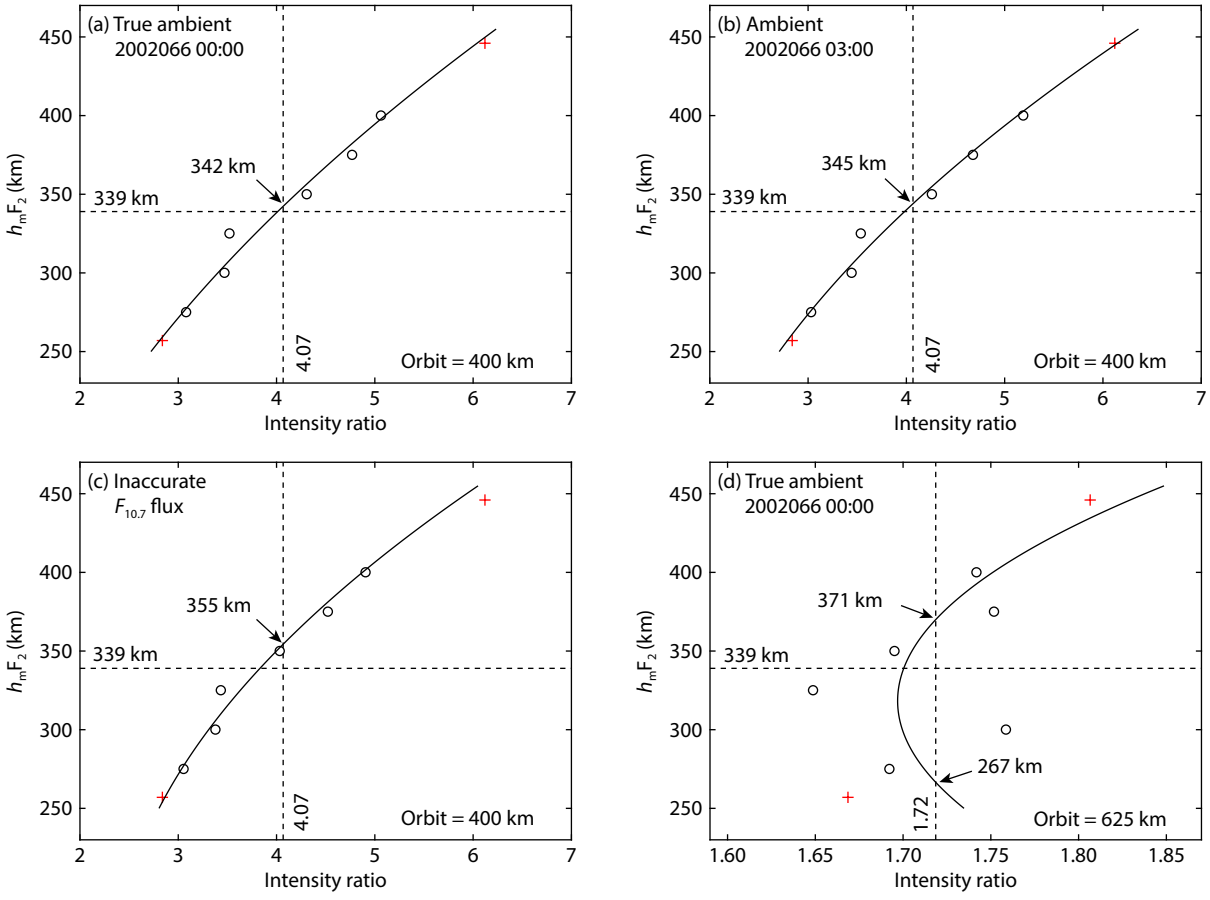

Figure 5. Retrieval of the peak height of the F_2 region (h_mF_2) by using the quadratic polynomial fitting (QPF) method. (a–c) The true atmospheric conditions (i.e., T_n, n_O, and n_{O_2}) are associated with 2002066 00:00 local time (LT) at [0°N, 0°E], the true h_mF_2 is 339 km, and the true intensity ratio is 4.07. (a) Circles: Intensity ratios calculated by using six pairs of electron and O^+ density profiles with various h_mF_2. In these calculations, the true atmospheric conditions are assumed to be known. Solid line: The quadratic polynomial obtained by fitting the circles. (b–c) Same as (a), except that the atmospheric conditions used in the calculation of the intensity ratios are associated with (b) 2002066 03:00 LT at [0°N, 0°E], and (c) 00:00 LT at [0°N, 0°E], with a daily $F_{10.7}$ flux of 157 sfu and an 81-day mean value of 180 sfu (i.e., 20 sfu smaller than those of 2002066). The h_mF_2 retrieved from the polynomial fits are indicated in each panel by an arrow. (d) Same as (a), except that the observer is assumed to orbit at 625 km. In all four panels, the red plus signs are the intensity ratios associated with h_mF_2 of 255 and 445 km, which are simulated under the true atmospheric conditions associated with 2002066 00:00 LT at [0°N, 0°E].

atmospheric conditions (e.g., the neutral temperature and the O and O_2 density profiles) at the location and time of the observation by using the NRLMSIS 2.0 model. In practice, these model predictions will not agree perfectly with the real atmosphere. Under these predicted atmospheric conditions, we then use the radiative transfer models to simulate a small number of intensity ratios associated with a large range of specific h_mF_2, which are fitted to derive the quadratic polynomial. For this analysis, the specific h_mF_2 are chosen to be 275, 300, 325, 350, 375, and 400 km. The electron and O^+ density profiles associated with these h_mF_2 are generated at random locations and times by using the IRI 2016 model (i.e., the only constraint on the density profiles is the h_mF_2), which are precomputed to be used for all the cases shown in Figure 5. Random locations and times are used because we need to generate density profiles with the required h_mF_2 (the model cannot generate all the required h_mF_2 if the location and time are fixed). We have verified that the use of different random locations and times for the generation of the density profiles does not affect the retrieval accuracy.

In Figure 5a, we assume that the atmospheric conditions for finding the quadratic polynomial can be predicted accurately, namely that T_n, n_O, and n_{O_2} are the same as those used for the simulation of the true intensity ratio. In this case, the effects of multiple scattering and O_2 absorption can be accounted for accurately. Using the quadratic polynomial derived by fitting the modeled ratios, the h_mF_2 are estimated to be 342 km, with an error of only 3 km. However, as indicated earlier, although the NRLMSIS 2.0 model is expected to be fairly accurate under geomagnetically quiet times, in practice the modeled predictions will not agree perfectly with the actual atmosphere. Therefore, as shown in Figures 5b, c, we examine the retrieval accuracy when the atmospheric conditions are not predicted accurately. As illustrated in Figure 5b, we use the atmospheric conditions calculated by the NRLMSIS 2.0 model on 2002066 03:00 LT to find the quadratic polynomial. In Figure 5c, we assume a daily $F_{10.7}$ flux of 157 sfu and an 81-day mean flux of 180 sfu (i.e., 20 sfu smaller than those of 2002066) for calculating the atmospheric conditions with the NRLMSIS 2.0 model. In these two cases, the effects of multiple scattering and O_2 absorption cannot be accounted for accurately, leading to larger errors (6 and 16 km) in the retrieved h_mF_2.

For comparison, we model an observation at the same location and time as in Figure 5a from an orbit of 625 km, which leads to an intensity ratio of 1.72. We then attempt to retrieve the h_mF_2 by using the same method as discussed in Figure 5a. The results are shown in Figure 5d. The modeled ratios do not exhibit a clear quadratic relationship with h_mF_2. As a result, the QPF method leads to two solutions (267 and 371 km) that have errors of tens of kilometers compared with the true h_mF_2 of 339 km. In such a case, fitting the modeled ratios by using a linear relationship can produce a better and unique h_mF_2 estimate, which is 350 km (the linear fit is not shown in the figure). The error of this estimation is 11 km, which is still much larger than that (3 km) obtained in Figure 5a. This comparison indicates that in terms of retrieval accuracy, observations from an orbit of 400 km are better suited for h_mF_2 retrieval than are those from an orbit of 625 km.

As shown in Figure 5, we derive the quadratic polynomials by fitting the intensity ratios associated with h_mF_2 in the range of 275–400 km (i.e., the circles). The reason for not using a larger range of h_mF_2 (e.g., from 250 to 450 km) is to investigate whether some unusually large or unusually small h_mF_2 can be retrieved by using the QPF method. In other words, in the real ionosphere some h_mF_2 might be larger or smaller than the upper or lower limit of the NRLMSIS 2.0 model predictions. The question is whether the QPF method is applicable for such cases by means of extrapolation. To answer this question, we simulate two intensity ratios using the atmospheric conditions on 2002066 00:00 LT at [0°N, 0°E], which are associated with h_mF_2 of 255 and 445 km, respectively. The results are shown as red plus signs in Figure 5. Although the plus signs are not used during the fitting of the quadratic polynomials, they agree well with the fit. This result indicates that the QPF method can be applied with extrapolation to retrieve h_mF_2 that exceed the upper and lower limits of the NRLMSIS 2.0 model predictions. At the least, the method is valid for the typical range of nighttime $h_mF_2 \simeq$ 250–450 km.

In the analysis above, we have not considered the effect of measurement noise on the retrieval. Because the intensity ratios can readily be measured by using a pair of photometers, we investigate the effect of measurement noise on h_mF_2 retrieval by using the typical sensitivity and exposure time of the photometers that are currently in orbit for ionospheric remote sensing. The Ionospheric Photometer that is carried by the FengYun 3D meteorological satellite measures the 135.6 nm emission to estimate the nighttime n_mF_2; it has a sensitivity of ~150 counts/*Ra*/s at 135.6 nm and an exposure time of 10 s (Wang YG et al., 2022). For the results shown in Figure 5a, the true 130.4 and 135.6 nm emission intensities are 190.6 and 46.8 *Ra*, respectively, with a ratio of 4.07. We include Poisson noise in the two intensity values by using the sensitivity and exposure time of the Ionospheric Photometer. A total of 10,000 random realizations are modeled, from which 10,000 h_mF_2 are estimated. The mean and standard deviation of the 10,000 estimated h_mF_2, which are 342.3 ± 1.0 km, represent the accuracy and precision of the estimation. Owing to the large intensities, the SNRs are ~24–27 dB for the case analyzed above. For Poisson noise, the SNR decreases with intensity. If we reduce the intensities by an order of magnitude (i.e., 19.06 and 4.68 R), the SNRs are ~19–22 dB and the 10,000 estimated h_mF_2 have a mean and standard deviation of 342.3 ± 3.3 km. For intensities of 1.906 and 0.468 *Ra*, the SNRs are ~14–17 dB, and the mean and standard deviation are 342.6 ± 10.3 km. These intensity values cover the typical range of the two emissions in the nighttime ionosphere. We find, based on the estimations above, that in ionospheric regions with weak emissions on the order of ~1.0 *Ra*, the measurement noise alone can lead to ~10 km errors in the retrieved h_mF_2, whereas in bright regions where the intensities are tens to hundreds of Rayleighs, the errors attributable to measurement noise are only ~1 km.

For comparison, we also estimate the retrieval accuracy from an orbit of 625 km. For this orbit, the true intensities are 100.7 and 58.6 R, respectively, with a ratio of 1.72 (see Figure 5d). For solution uniqueness, the linear fit derived from Figure 5d is used to retrieve the h_mF_2 instead of the quadratic polynomial. With the Poisson noise included, the mean and standard deviation of the

10,000 retrieved h_mF_2 are 349.5 ± 23.5 km. If the intensity is reduced by one (or two) orders of magnitude, the retrieved h_mF_2 is 350.7 ± 73.9 km (354.2 ± 230.2 km). Apparently, the errors attributable to measurement noise are much larger for the orbit of 625 km than for the orbit of 400 km.

3.3.2 The table lookup method

As discussed in Section 3.3.1, in the QPF method the retrieval of h_mF_2 from an individual ratio requires first-principles simulations under specific atmospheric and ionospheric conditions that are associated with the location and time of the observation. Such a method can make the best use of predictions of the atmospheric and ionospheric conditions from empirical or physical models; thus, it is expected to be able to retrieve h_mF_2 with relatively high accuracy. However, owing to the computationally expensive first-principles simulations, the QPF method is more suitable for processing the data on the ground. In comparison, table lookup methods are usually computationally much more efficient and can be used for on-orbit processing to obtain real-time monitoring of the h_mF_2. In such methods, first-principles simulations are performed to generate a precomputed table with which observations are compared, saving an enormous amount of time for on-orbit data processing to enable real-time retrievals of h_mF_2. One of the best-known table lookup methods for far-ultraviolet remote sensing was developed by Strickland et al. (1995) to retrieve the column O/N_2 density ratio from the 135.6/Lyman–Birge–Hopfield intensity ratio. In this section, we describe a table lookup method for the retrieval of the nighttime h_mF_2 from the 130.4/135.6 nm intensity ratio. It should be emphasized that no standard procedures or unique techniques exist for the development of such methods, meaning that various table lookup methods (with different retrieval accuracies) can be developed for the same purpose. The table lookup method that we develop in this study is for illustrative purposes, which are used to further demonstrate that observations from an orbit of 400 km are better suited for h_mF_2 retrieval than are those from an orbit of 625 km.

In our method, we establish a lookup table by simulating a large number of nadir intensities associated with various h_mF_2. If the table is sufficiently large, it should be able to encompass a nearly complete set of relations between h_mF_2 and the intensity ratios. We can then retrieve the h_mF_2 based on comparison of the observations and the tabulated ratios. Because the atmospheric conditions have large effects on the relationship between the h_mF_2 and the intensity ratios (through multiple scattering and O_2 absorption), in practice a series of tables can be established for various solar conditions (e.g., one table can be generated for a specific solar $F_{10.7}$ flux). More specifically, to retrieve the h_mF_2 from intensity ratios observed under specific solar conditions, we use the radiative transfer models and the empirical models to generate a large table that contains intensities versus h_mF_2 that are associated with different locations and times over the entire nighttime ionosphere. Once the table is generated, we can search the table for a limited number (e.g., 100) of intensity ratios that are closest to the observed ones. Among these selected intensity ratios, we further search for a smaller number (e.g., 10) of intensity ratios whose related 135.6 nm (or 130.4 nm) intensities are closest to the observed one. We then take the mean of the 10 corresponding h_mF_2, which is considered the retrieved h_mF_2. In this way, the h_mF_2 is retrieved based on the ratio and one of the two intensities, so the table should record the absolute intensities (instead of only their ratios) versus h_mF_2. Note that the table does not contain information about the locations and times of those modeled ratios such that the observed ratios at a specific location and time are compared with modeled ratios associated with all locations and times in the nighttime ionosphere. Such a statistical comparison is made to ensure that a sufficiently large number of cases in the table are associated with various atmospheric and ionosphere conditions for comparison with a specific observed ratio (i.e., the table should contain a nearly complete set of relations between the h_mF_2 and the ratios, which cannot be established if the location and time are fixed to be the same as the specific observation).

One of the main differences between the QPF method and the table lookup method is that in the former, we use the ambient atmospheric conditions modeled by the NRLMSIS 2.0 model at the exact locations and times of the observations for the retrieval, whereas in the latter, the retrieval is based on a statistical comparison of the observations and the tabulated ratios that are precomputed for a large number of locations and times (i.e., not for the exact locations and times of the observations). Thus, the retrieval accuracy of the table lookup method, which is computationally efficient, is expected to be lower than the computationally expensive QPF method.

As shown in Figure 6, we retrieve the global distribution of the h_mF_2 from the intensity ratios shown in Figure 2d by using the table lookup method. The true h_mF_2 are shown in Figure 2c, which are associated with 2002066 00:00 LT. Because in practice we cannot predict the real-time atmospheric conditions accurately when using the NRLMSIS 2.0 model, we generate a lookup table, using the atmospheric conditions associated with 2002066 03:00 LT to mimic the practical situation. In other words, the lookup table is generated by using the results shown in Figures 2f–j. By comparing Figures 6a, c with Figure 2c, we find that the h_mF_2 can be retrieved from the intensity ratios observed at 400 km with errors less than ~20 km. In comparison, the errors in the h_mF_2 retrieved from the intensity ratios observed from 625 km can be as large as ~80 km, which is nearly the same as the variability of the h_mF_2 (~300−380 km) during the nighttime of 2002066. Indeed, the global variation in the h_mF_2 can be reconstructed well from the intensity ratios observed from 400 km (see Figure 6a), which is not true for the case of 625 km (see Figure 6c). This result confirms that in terms of retrieval accuracy, observations from an orbit of 400 km are better suited to estimating the h_mF_2 in the nighttime ionosphere than are those at 625 km.

Note that although the two numerical algorithms discussed in Section 3.3 cannot be used to retrieve the h_mF_2 from an orbit of 625 km (or from higher orbits), it does not mean that with the development of more dedicated algorithms, h_mF_2 retrieval cannot be achieved for those high orbits. Indeed, observations from higher orbits, such as those from the geostationary orbit, can monitor the global variations in the ionosphere with a high temporal resolution (Eastes et al., 2017, 2020) and are better than an orbit of 400 km in this regard. However, in this study we focus on comparing the retrieval accuracies from different orbits and

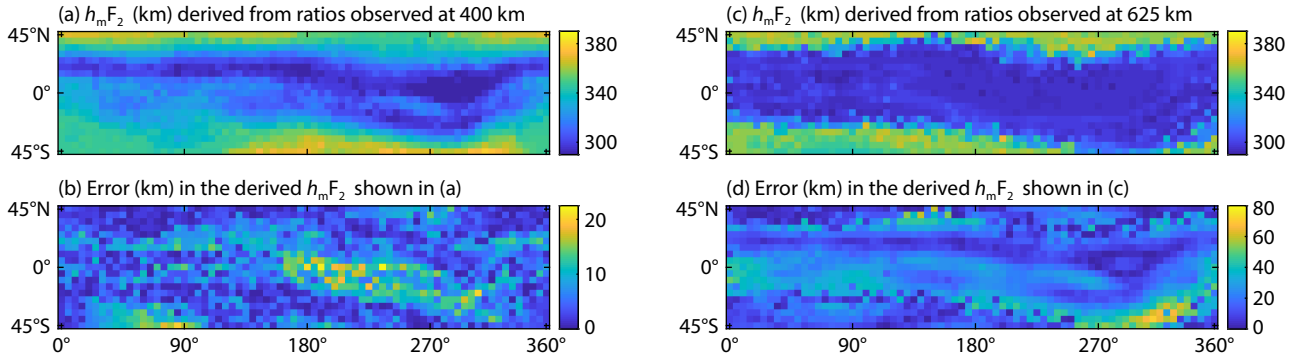

Figure 6. Retrieval of the peak height of the F_2 region (h_mF_2) when using the table lookup method. (a–b) The h_mF_2 retrieved from the intensity ratios shown in Figure 2d when using the table lookup method, and the errors in the retrieved h_mF_2 (defined as the absolute difference between the retrieved h_mF_2 and the true h_mF_2). (c–d) The h_mF_2 retrieved from the intensity ratios shown in Figure 2e by using the table lookup method, and the errors in the retrieved h_mF_2. The altitudes of the orbits are (a–b) 400 km and (c–d) 625 km, respectively.

leave the development of those more dedicated algorithms for future studies.

3.4 Comparison of Model, Ionosondes, and GUVI Observations

So far, our investigations are based purely on numerical simulations. In those simulations, we demonstrate that the QPF or the table lookup method can be used to retrieve the h_mF_2 observed from an orbit of 400 km with high accuracy. However, the performance of these methods in analyzing actual data is not known. Unfortunately, no observations from ~400 km are currently available, so the methods cannot be further validated. Future observations from a low-altitude platform, such as the International Space Station, the Chinese Space Station, or the FengYun satellites are required for validation. As for higher orbits, the GUVI has been routinely monitoring the 130.4 and 135.6 nm emissions from an orbit of ~625 km for more than two decades (Paxton et al., 1999). The GUVI is a hyperspectral imager that is capable of measuring the entire far-ultraviolet spectrum from ~115 to 180 nm with a 1.9 nm resolution (Meier et al., 2015). However, the sensitivity of the GUVI near 135.6 nm is only approximately 0.115 counts/*Ra*/s. As discussed in Section 3.3, in the case of low SNRs, the errors in the h_mF_2 retrieved from intensity ratios observed at 625 km are tens to hundreds of kilometers. Therefore, our algorithms discussed in Section 3.3 cannot be used to retrieve h_mF_2 from the 130.4/135.6 nm intensity ratios observed by the GUVI.

To further show the difficulty of estimating h_mF_2 from the GUVI ratios, we have compared the nighttime h_mF_2 measured by ionosondes with the coinciding GUVI observations from 2013 to 2015. The results are shown in Figure 7. These h_mF_2 data are obtained from the Global Ionospheric Radio Observatory (GIRO) database (Reinisch and Galkin, 2011). The information on the 14 stations used in the comparison are given in Table 3. All are located at mid to low latitudes between 45°S and 45°N. The coinciding ionosonde and GUVI observations are determined by comparing their geographic locations. Specifically, if a GUVI ratio is associated with a geographic location that is within 0.4° latitude and 0.4° longitude around any of the 14 ionosonde stations, it is considered coincide geographically. The temporal resolution of the ionosonde measurements is approximately 10 min, which is

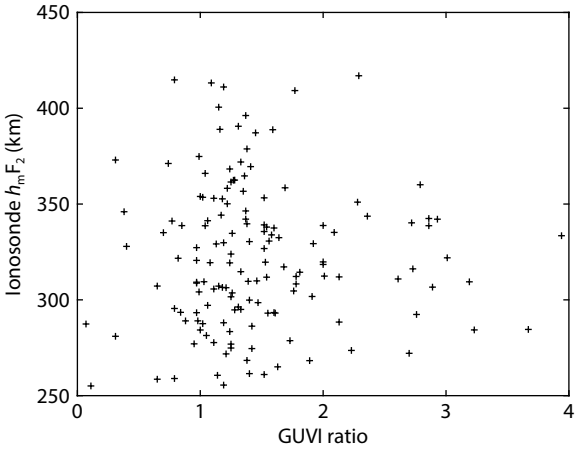

Figure 7. Coinciding observations of the nighttime peak height of the F_2 region (h_mF_2) by ionosondes and the 130.4/135.6 nm intensity ratios by the Global Ultraviolet Imager (GUVI) from 2013 to 2015.

interpolated by using the time of the GUVI observations to achieve the comparison shown in Figure 7. Indeed, no clear relationship between the ionosonde h_mF_2 and the GUVI ratios can be found.

Although it is difficult to retrieve h_mF_2 from the GUVI observations, they can be compared with the models to investigate similarities and differences. In Figure 8, we compare the GUVI observations from March 4 to 7, 2002, with simulations using the NRLMSIS 2.0 and IRI 2016 models. Figures 8a–c show the observations and Figures 8d–h show the modeling results. During this period of time, the daily $F_{10.7}$ flux and its 81-day mean value are ~175 sfu and ~200 sfu, respectively, and $Ap \leq 20$. By comparing Figures 8a, b with Figures 8e, f, we find that the global structures of the modeled and observed intensities are morphologically similar and are determined by the global distribution of the n_mF_2 (see Figure 8g). Moreover, the absolute intensity values of the model and observations are comparable. However, the observed intensity maps seem to show the South Atlantic Anomaly, which is not seen in the modeling results. Figures 8c, d show that the observed and modeled intensity ratios are also morphologically similar, indicating that the global variation in the h_mF_2 during these days should

be similar to the model prediction shown in Figure 8h. However, the geographical variations in the observed ratios are not as clear as the modeled ratios, likely because of the low SNRs of the observations.

Figure 9 shows another comparison of the models and observations by using the GUVI data observed from March 2 to 5, 2014. For this period of time, the daily $F_{10.7}$ flux and its 81-day mean value are ~130 sfu and ~140 sfu, respectively, and $Ap \leq 6$. Note that the scan mirror on the GUVI failed in December 2007. Since then, the GUVI has operated only in the spectrographic mode with the mirror held in a fixed direction, approximately 47° from nadir in the direction away from the Sun. The instantaneous pixel integration time was increased from 0.068 to 3 s, which means that the SNR of the observations is improved by nearly 50 times. With the higher SNR, the geographical variations of the observed intensities and ratios can be more clearly seen in Figure 9 compared with those shown in Figure 8. Specifically, the similarities between the observed and modeled ratios are much more apparent in Figures 9c, d. However, in Figure 9 the observed ratios have a larger variability (~1.0–1.6) than do the modeled ratios (~1.1–1.3), which might be due to the larger variability in the actual ionosphere when compared with the modeled ionosphere or to additional source emissions from the impact of conjugate photoelectrons.

We emphasize that although the comparisons shown in Figures 8–9 demonstrate similarities between the models and observations, they cannot be used to validate the new remote sensing strategy proposed in this study (i.e., nighttime h_mF_2 can be retrieved from the intensity ratios observed from an orbit of 400 km) because the GUVI observations were acquired from an orbit of 625 km. Ideally, our study can motivate future observations from an orbit of 400 km to verify the new strategy as well as the

Table 3. Information on the ionosonde stations used in our analysis.

USRI code	Station name	Latitude	Longitude
KJ609	KWAJALEIN	9.0°N	167.2°E
GU513	GUAM	13.6°N	144.9°E
PRJ18	RAMEY	18.5°N	292.9°E
LM42B	LEARMONTH	21.8°N	114.1°E
AU930	AUSTIN	30.4°N	262.3°E
EG931	EGLIN AFB	30.5°N	273.5°E
PA836	PT ARGUELLO	34.8°N	239.5°E
GR13L	GRAHAMSTOWN	33.3°N	26.5°E
SA418	SANYA	18.3°N	109.4°E
WU430	WUHAN	30.5°N	114.4°E
BVJ03	BOA VISTA MELROSE	2.9°N	299.3°E
ME929	MELROSE	29.7°N	278.0°E
LV12P	LOUISVALE	28.5°S	21.2°E
HE13N	HERMANUS	34.4°S	19.2°E

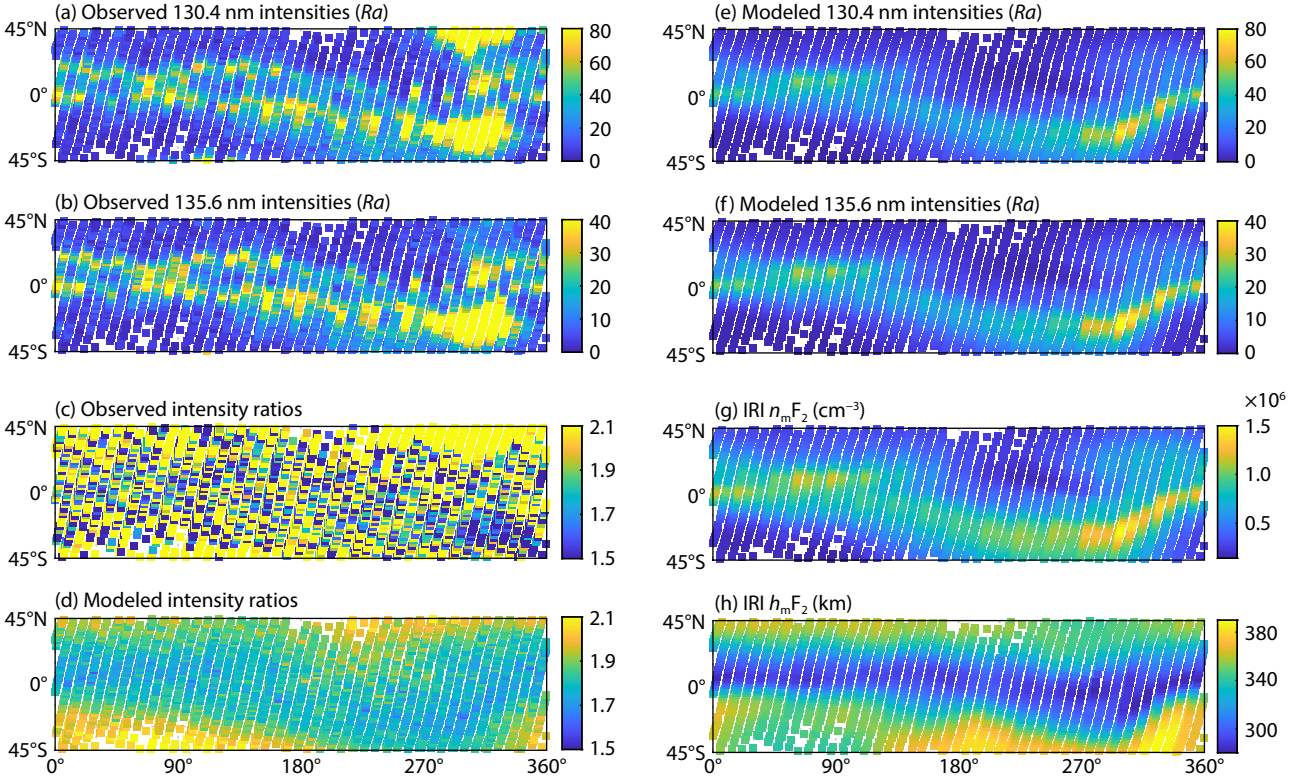

Figure 8. Comparison of simulations with Global Ultraviolet Imager (GUVI) observations. (a–c) The absolute intensities and ratios of the 130.4 and 135.6 nm emissions observed by the GUVI from March 4 to 7, 2002 (i.e., 2002063-066). (d–f) The modeled intensities and ratios when using the NRLMSIS 2.0 and International Reference Ionosphere (IRI) 2016 models with the same geographic locations and times as those shown in (a–c). (g–h) The peak density (n_mF_2) and peak height of the F_2 region (h_mF_2) predicted by the IRI 2016 model.

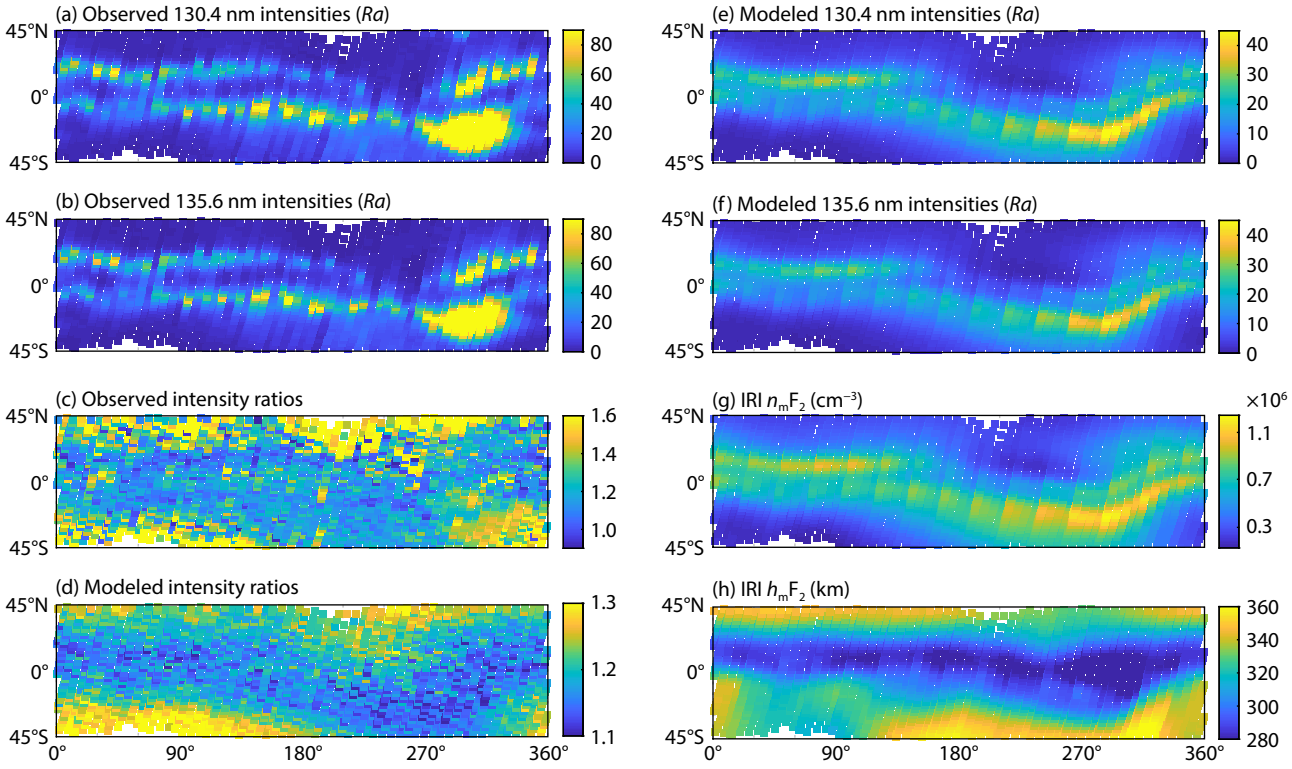

Figure 9. Same as Figure 8, except that the emissions are observed or modeled for March 2–5, 2014 (i.e., 2014061-064).

QPF method and the table lookup method.

4. Conclusions

In this study, through mostly numerical simulations, we investigate the statistical and global characteristics of the 130.4/135.6 nm airglow intensity ratios and propose a new strategy for the use of these ratios for remote sensing of the nighttime ionosphere. Our modeling results show that the intensity ratios and their variability are sensitive to the altitude from which the emissions are observed. When the observer is orbiting at an altitude of 400 km, which is within the typical range of nighttime $h_mF_2 \simeq$ 250–450 km, a roughly quadratic relationship between h_mF_2 and the intensity ratios can be established. We have developed two numerical methods, named the QPF method and the table lookup method, for the retrieval of h_mF_2 from the intensity ratios. By using these methods to retrieve h_mF_2 from synthetic observations, we have found that the h_mF_2 can be retrieved with errors of only a few kilometers (up to ~20 km) in the case when the observer orbits at 400 km. In comparison, the errors in the retrieved h_mF_2 are typically tens to hundreds of kilometers when the ratios are observed from an orbit of 625 km. We propose that in terms of retrieval accuracy, observations from an orbit of 400 km (or from a similar orbit that is within the typical range of nighttime $h_mF_2 \simeq$ 250–450 km) are better suited for the estimation of nighttime h_mF_2 than are observations from higher orbits. Our findings pave the way for the use of the 130.4/135.6 nm airglow intensity ratios for remote sensing of the nighttime ionosphere.

Acknowledgments

This work was supported by the National Natural Science Foundation of China through Grant 8206100245 and by the Chinese Meteorological Administration through Grant FY-APP-ZX-2022.0222. The GUVI data were provided through support from the NASA Mission Operations and Data Analysis (MO&DA) program and are available from http://guvitimed.jhuapl.edu/data_products. The GUVI instrument was designed and built by the Aerospace Corporation and Johns Hopkins University based on the design of the Defense Meteorological Satellite Program (DMSP) Special Sensor Ultraviolet Spectrographic Imager (SSUSI). The principal investigator is Andrew B. Christensen, and the chief scientist and co-principal investigator is Larry J. Paxton. The GIRO data are publicly available from http://spase.info/SMWG/Observatory/GIRO.

References

Ahmed, S. M., Kanik, I., and Link, R. (1996). Temperature-dependent photoabsorption cross section measurements of O_2 at the OI-1304 Å triplet emission lines. *Chem. Phys. Lett.*, *259*(5–6), 545–553. https://doi.org/10.1016/0009-2614(96)00783-x

Bilitza, D., Altadill, D., Truhlik, V., Shubin, V., Galkin, I., Reinisch, B., and Huang, X. (2017). International Reference Ionosphere 2016: From ionospheric climate to real-time weather predictions. *Space Weather*, *15*(2), 418–429. https://doi.org/10.1002/2016sw001593

DeMajistre, R., Paxton, L. J., Morrison, D., Yee, J. H., Goncharenko, L. P., and Christensen, A. B. (2004). Retrievals of nighttime electron density from Thermosphere Ionosphere Mesosphere Energetics and Dynamics (TIMED) mission Global Ultraviolet Imager (GUVI) measurements. *J. Geophys. Res.: Space Phys.*, *109*(A5), A05305. https://doi.org/10.1029/2003ja010296

DeMajistre, R., Brandt, P. C., Immel, T. J., Yee, J. H., Dalgarno, A., Paxton, L. J., and Kharchenko, V. (2005). Storm-time enhancement of mid-latitude ultraviolet emissions due to energetic neutral atom precipitation. *Geophys. Res. Lett.*, *32*(15), L15105. https://doi.org/10.1029/2005gl023059

Dymond, K. F., Thonnard, S. E., McCoy, R. P., and Thomas, R. J. (1997). An optical remote sensing technique for determining nighttime *F* region electron

density. *Radio Sci.*, *32*(5), 1985–1996. https://doi.org/10.1029/97rs01887

Dymond, K. F. (2009). Remote sensing of nighttime *F* region peak height and peak density using ultraviolet line ratios. *Radio Sci.*, *44*(1), RS0A28. https://doi.org/10.1029/2008rs004091

Eastes, R. W., McClintock, W. E., Burns, A. G., Anderson, D. N., Anderson, L., Codrescu, M., Correira, J. T., Daniell, R. E., England, S. L., … Oberheide, J. (2017). The global-scale observations of the limb and disk (GOLD) mission. *Space Sci. Rev.*, *212*(1–2), 383–408. https://doi.org/10.1007/s11214-017-0392-2

Eastes, R. W., McClintock, W. E., Burns, A. G., Anderson, D. N., Andersson, L., Aryal, S., Budzien, S. A., Cai, X., Codrescu, M. V., … Woods, T. N. (2020). Initial observations by the GOLD mission. *J. Geophys. Res.*: *Space Phys.*, *125*(7), e2020JA027823. https://doi.org/10.1029/2020ja027823

Emmert, J. T., Drob, D. P., Picone, J. M., Siskind, D. E., Jones, Jr. M., Mlynczak, M. G., Bernath, P. F., Chu, X., Doornbos, E., … Yuan, T. (2021). NRLMSIS 2.0: A whole-atmosphere empirical model of temperature and neutral species densities. *Earth Space Sci.*, *8*(3), e2020EA001321. https://doi.org/10.1029/2020ea001321

Fu, L. P., Peng, R. Y., Shi, E. T., Peng, J. L., Wang, T. F., Jiang, F., Jia, N., Li, X. Y., and Wang, Y. M. (2015). Far ultraviolet nighttime ionospheric photometer. *Astrophys. Space Sci.*, *355*(1), 1–7. https://doi.org/10.1007/s10509-014-2139-9

Gérard, J. C., Anderson, D. N., and Matsushita, S. (1977). Magnetic storm effects on the tropical ultraviolet airglow. *J. Geophys. Res.*: *Space Phys.*, *82*(7), 1126–1136. https://doi.org/10.1029/JA082i007p01126

Gibson, S. T., and Lewis, B. R. (1996). Understanding diatomic photodissociation with a coupled-channel Schrodinger equation model. *J. Electron Spectros. Relat. Phenom.*, *80*, 9–12. https://doi.org/10.1016/0368-2048(96)02910-6

Kamalabadi, F., Qin, J. Q., Harding, B. J., Iliou, D., Makela, J. J., Meier, R. R., England, S. L., Frey, H. U., Mende, S. B., and Immel, T. J. (2018). Inferring nighttime ionospheric parameters with the far ultraviolet imager onboard the ionospheric connection explorer. *Space Sci. Rev.*, *214*(4), 70. https://doi.org/10.1007/s11214-018-0502-9

Kil, H., DeMajistre, R., and Paxton, L. J. (2004). *F*-region plasma distribution seen from TIMED/GUVI and its relation to the equatorial spread *F* activity. *Geophys. Res. Lett.*, *31*(5), L05810. https://doi.org/10.1029/2003gl018703

Kil, H., Schaefer, R. K., Paxton, L. J., and Jee, G. (2020). The far ultraviolet signatures of conjugate photoelectrons seen by the special sensor ultraviolet spectrographic imager. *Geophys. Res. Lett.*, *47*(1), e2019GL086383. https://doi.org/10.1029/2019gl086383

Lei, J. H., Liu, L. B., Wan, W. X., and Zhang, S. R. (2005). Variations of electron density based on long-term incoherent scatter radar and ionosonde measurements over Millstone Hill. *Radio Sci.*, *40*(2), RS2008. https://doi.org/10.1029/2004rs003106

Meier, R. R., and Lee, J. S. (1982). An analysis of the OI 1304 A dayglow using a Monte Carlo resonant scattering model with partial frequency redistribution. *Planet. Space Sci.*, *30*(5), 439–450. https://doi.org/10.1016/0032-0633(82)90053-8

Meier, R. R. (1991). Ultraviolet spectroscopy and remote sensing of the upper atmosphere. *Space Sci. Rev.*, *58*(1), 1–185. https://doi.org/10.1007/bf01206000

Meier, R. R., Picone, J. M., Drob, D., Bishop, J., Emmert, J. T., Lean, J. L., Stephan, A. W., Strickland, D. J., Christensen, A. B., … Gibson, S. T. (2015). Remote sensing of Earth's limb by TIMED/GUVI: Retrieval of thermospheric composition and temperature. *Earth Space Sci.*, *2*(1), 1–37. https://doi.org/10.1002/2014ea000035

Meléndez-Alvira, D. J., Meier, R. R., Picone, J. M., Feldman, P. D., and McLaughlin, B. M. (1999). Analysis of the oxygen nightglow measured by the Hopkins Ultraviolet Telescope: Implications for ionospheric partial radiative recombination rate coefficients. *J. Geophys. Res.*: *Space Phys.*, *104*(A7), 14901–14913. https://doi.org/10.1029/1999ja900136

Paxton, L. J., Christensen, A. B., Humm, D. C., Ogorzalek, B. S., Pardoe, C. T., Morrison, D., Weiss, M. B., Crain, W., Lew, P. H., … Meng, C. I. (1999). Global Ultraviolet Imager (GUVI): Measuring composition and energy inputs for the NASA Thermosphere Ionosphere Mesosphere Energetics and Dynamics (TIMED) mission. In *Proceedings of the SPIE, Optical Spectroscopic Techniques and Instrumentation for Atmospheric and Space Research III* (pp. 265–276). Denver, USA: SPIE. https://doi.org/10.1117/12.366380

Qian, L. Y., Burns, A. G., Emery, B. A., Foster, B., Lu, G., Maute, A., Richmond, A. D., Roble, R. G., Solomon, S. C., and Wang, W. (2013). The NCAR TIE-GCM: A community model of the coupled thermosphere/ionosphere system. *Geophys. Monogr. Ser.*, *201*, 73–83. https://doi.org/10.1029/2012GM001297

Qin, J. Q., Makela, J. J., Kamalabadi, F., and Meier, R. R. (2015). Radiative transfer modeling of the OI 135.6 nm emission in the nighttime ionosphere. *J. Geophys.*: *Res. Space Phys.*, *120*(11), 10116–10135. https://doi.org/10.1002/2015ja021687

Qin, J. Q., Kamalabadi, F., and Makela, J. J. (2016). Quantifying the inversion accuracy of simplified physical models for the nighttime OI 135.6 nm emission. *J. Geophys. Res.*: *Space Phys.*, *121*(6), 5805–5814. https://doi.org/10.1002/2016ja022720

Qin, J. Q. (2020). Far ultraviolet remote sensing of the nighttime ionosphere using the OI 130.4-nm emission. *J. Geophys. Res.*: *Space Phys.*, *125*(6), e2020JA028049. https://doi.org/10.1029/2020ja028049

Qin, J. Q., and Harding, B. J. (2020). A comparative analysis of the OI 130.4-nm emission observed by NASA's TIMED mission using a Monte Carlo radiative transfer model. *J. Geophys. Res.*: *Space Phys.*, *125*(1), e2019JA027520. https://doi.org/10.1029/2019ja027520

Rajesh, P. K., Liu, J. Y., Hsu, M. L., Lin, C. H., Oyama, K. I., and Paxton, L. J. (2011). Ionospheric electron content and NmF2 from nighttime OI 135.6 nm intensity. *J. Geophys. Res.*: *Space Phys.*, *116*(A2), A02313. https://doi.org/10.1029/2010ja015686

Reinisch, B. W., and Galkin, I. A. (2011). Global ionospheric radio observatory (GIRO). *Earth, Planets Space*, *63*(4), 377–381. https://doi.org/10.5047/eps.2011.03.001

Stephan, A. W., Chakrabarti, S., Dymond, K. F., Budzien, S. A., Thonnard, S. E., and McCoy, R. P. (2001). Far ultraviolet equatorial aurora during geomagnetic storms as observed by the Low-Resolution Airglow and Aurora Spectrograph. *J. Geophys. Res.*: *Space Phys.*, *106*(A12), 30323–30330. https://doi.org/10.1029/2001ja001103

Strickland, D. J., and Anderson, D. E. (1977). OI 1304-Å nadir intensity/column production rate ratio and its application to airglow studies. *J. Geophys.*: *Res. Space Phys.*, *82*(7), 1013–1016. https://doi.org/10.1029/JA082i007p01013

Strickland, D. J., Evans, J. S., and Paxton, L. J. (1995). Satellite remote sensing of thermospheric O/N_2 and solar EUV: 1. Theory. *J. Geophys. Res.*: *Space Phys.*, *100*(A7), 12217–12226. https://doi.org/10.1029/95JA00574

Strickland, D. J., Bishop, J., Evans, J. S., Majeed, T., Shen, P. M., Cox, R. J., Link, R., and Huffman, R. E. (1999). Atmospheric Ultraviolet Radiance Integrated Code (AURIC): Theory, software architecture, inputs, and selected results. *J. Quant. Spectrosc. Radiat. Transf.*, *62*(6), 689–742. https://doi.org/10.1016/s0022-4073(98)00098-3

Sun, L. C., Xu, J. Y., Zhu, Y. J., Yuan, W., and Zhao, X. K. (2021). Case study of an Equatorial Plasma Bubble Event investigated by multiple ground-based instruments at low latitudes over China. *Earth Planet. Phys.*, *5*(5), 435–449. https://doi.org/10.26464/epp2021048

Wang, Y. G., Fu, L. P., Jiang, F., Hu, X. Q., Liu, C. B., Zhang, X. X., Li, J. W., Ren, Z. P., He, F., … Mao, T. (2022). Far-ultraviolet airglow remote sensing measurements on Feng Yun 3-D meteorological satellite. *Atmos. Meas. Tech.*, *15*(5), 1577–1586. https://doi.org/10.5194/amt-15-1577-2022

Wautelet, G., Hubert, B., Gérard, J. C., and Immel, T. J. (2019). The OI-135.6 nm nighttime emission in ICON-FUV images: A new tool for the observation of classical medium-scale traveling ionospheric disturbances?. *J. Geophys. Res.*: *Space Phys.*, *124*(9), 7670–7686. https://doi.org/10.1029/2019ja026930

Wautelet, G., Hubert, B., Gérard, J. C., Immel, T. J., Frey, H. U., Mende, S. B., Kamalabadi, F., Kamaci, U., and England, S. L. (2021). First ICON-FUV nighttime NmF2 and hmF2 comparison to ground and space-based measurements. *J. Geophys. Res.*: *Space Phys.*, *126*(11), e2021JA029360. https://doi.org/10.1029/2021ja029360

Zhang, Y. L., Paxton, L. J., Kozyra, J. U., Kil, H., and Brandt, P. C. (2006). Nightside thermospheric FUV emissions due to energetic neutral atom precipitation during magnetic superstorms. *J. Geophys. Res.*: *Space Phys.*, *111*(A9), A09307. https://doi.org/10.1029/2005ja011152

Zhang, Y. L., and Paxton, L. J. (2019). Observations of conjugated ring current auroras at subauroral latitudes. *J. Atmos. Sol. Terr. Phys.*, *184*, 1–4. https://doi.org/10.1016/j.jastp.2019.01.005